

# Detection of a Stellar Stream Behind Open Cluster NGC 188: Another Part of the Monoceros Stream<sup>†</sup>

Dana I. Casetti-Dinescu<sup>1,2</sup>, Terrence M. Girard<sup>1</sup>, Imants Platais<sup>3</sup> and William F. van  
Altena<sup>1</sup>

dana.casetti@yale.edu

## ABSTRACT

We present results from a WIYN/OPTIC photometric and astrometric survey of the field of the open cluster NGC 188 ( $(l,b) = (122.8^\circ, 22.5^\circ)$ ). We combine these results with the proper-motion and photometry catalog of Platais et al. and demonstrate the existence of a stellar overdensity in the background of NGC 188. The theoretical isochrone fits to the color-magnitude diagram of the overdensity are consistent with an age between 6 and 10 Gyr and an intermediately metal poor population ( $[Fe/H] = -0.5$  to  $-1.0$ ). The distance to the overdensity is estimated to be between 10.0 and 12.6 kpc. The proper-motions indicate that the stellar population of the overdensity is kinematically cold.

The distance estimate and the absolute proper motion of the overdensity agree reasonably well with the predictions of the Peñarrubia et al. model of the formation of the Monoceros stream. Orbits for this material constructed with plausible radial-velocity values, indicate that dynamically, this material is unlikely to belong to the thick disk. Taken together, this evidence suggests that the newly-found overdensity is part of the Monoceros stream.

*Subject headings:* Galaxy: structure — Galaxy: kinematics and dynamics — Galaxy: halo

---

<sup>1</sup>Astronomy Department, Yale University, P.O. Box 208101, New Haven, CT 06520-8101, USA

<sup>2</sup>Astronomical Institute of the Romanian Academy, Str. Cutitul de Argint 5, RO-75212, Bucharest 28, Romania

<sup>3</sup>Department of Physics and Astronomy, Johns Hopkins University, 3400 North Charles Street, Baltimore, MD 21218

<sup>†</sup>Paper 42 of the WIYN Open Cluster Study (WOCS).

## 1. Introduction

In the last decade, large-scale surveys have demonstrated the existence of extended tidal streams and overdensities that are believed to be generated by the disruption of massive systems such as dwarf galaxies as they merge with our Galaxy. To date, there are three reasonably well-documented large structures known to reside in the halo and outer disk of the Galaxy: the Sagittarius stream with its known progenitor the Sagittarius dwarf galaxy (Ibata et al. 1994, Ibata et al. 2001, Newberg et al. 2002, Majewski et al. 2003), the Monoceros stream (Newberg et al. 2002, Yanny et al. 2003, Ibata et al. 2003, Rocha-Pinto et al. 2003, Conn et al. 2005, 2007, 2008) with the much-disputed possible progenitor the overdensity in Canis Major, and finally the Virgo Overdensity (Newberg et al. 2002, Vivas & Zinn 2003, Jurić et al. 2008) with no known progenitor (see however Casetti-Dinescu et al. 2009 for a tentative suggestion). These structures’ formation has direct implications on the history of the assembling of the Milky Way and thus on the merger history in a  $\Lambda$ CDM cosmology.

Here we investigate a stellar overdensity found in the background of the open cluster NGC 188, and provide evidence that it is part of the Monoceros stream. Our data may help better constrain models of the formation and origin of this immense ring-like feature mapped from  $l = 60^\circ$  to  $300^\circ$ , above and below the Galactic plane (Conn et al. 2008 and references therein). In this investigation, we make use of the excellent absolute proper-motions and photometry catalog provided by Platais et al. (2003, hereafter P03) over an area of 0.75 square degrees down to  $V = 21$ . We also add new, deep  $VI$  photometry for an area half that of P03 obtained with WIYN 3.5m<sup>1</sup>, that reaches  $V \sim 23.5$ .

We present our data in Section 2, the color-magnitude diagram (CMD) interpretation in Section 3, the proper-motion analysis in Section 4, and discuss the origin of this newly-found overdensity in Section 5. In Section 6 we summarize our results.

## 2. The Data

In this work we use the  $BV$  photometry and proper-motion data from P03, and the  $VI$  photometry obtained during a 3-night run in October 2007 at WIYN with the Orthogonal Parallel Transfer Imaging Camera (OPTIC). The WIYN data were designed to cover a large area in the cluster region with the intent to: 1) better characterize the stellar overdensity

---

<sup>1</sup>The WIYN Observatory is a joint facility of the University of Wisconsin-Madison, Indiana University, Yale University and the National Optical Astronomy Observatory.

found in the P03 data, and 2) combine with a previous WIYN/OPTIC dataset taken in 2003 to characterize the astrometric properties and the proper-motion precision that can be obtained with this set-up. The astrometric aspect of the WIYN/OPTIC data set will be the subject of another paper, as part of a study that aims to characterize a similar type of detector with an area coverage of one square degree to be installed on WIYN early in 2010 and known as the One Degree Imager (ODI, Jacoby et al. 2002).

In Figure 1 we show the area coverage of the P03 catalog (the round area), our WIYN/OPTIC dataset (in gray), and the *VI* calibration field which is the data from von Hippel & Sarajedini (1998) (in black). Our data set covers 53% of the P03 area.

## 2.1. The Platais et al. Catalog

The P03 data include calibrated CCD *BV* photometry and proper-motions down to a limiting magnitude of  $V \sim 21$  for an area of 0.75 square degrees. A star/galaxy classification is also provided which lists 100 galaxies. The proper motions were derived from a combination of photographic plates and KPNO 4m Mosaic Imager data spanning 40 years. Proper-motion uncertainties are  $0.15 \text{ mas yr}^{-1}$  for well-measured objects, i.e., to  $V \sim 15$ , and below  $1.0 \text{ mas yr}^{-1}$  down to  $V \sim 20$ . The CMD from the P03 photometry clearly shows a main sequence-like feature (see Fig 8 in P03) between  $V = 19$  and 21, and  $B - V = 0.4$  to 0.8. This feature stimulated us to obtain a deeper, large-area data set. Other deep photometric studies of NGC 188 have not captured this feature, as they were concentrated on small areas on the cluster. Studies with somewhat larger areas are too shallow to sample the feature.

## 2.2. The WIYN/OPTIC Data

We have imaged an area of  $\sim 40' \times 40'$  around NGC 188 using overlapping OPTIC frames. This camera is able to compensate for real-time image motion providing tip/tilt corrections without additional optics or moving parts via orthogonal transfer shifting of the charge (Tonry et al. 1997) thus effectively improving the seeing. It consists of two 2K by 4K orthogonal transfer CCDs mounted adjacent to each other in a single dewar. Each CCD is electronically divided into two regions, and each of these regions has two parts: a guide region and a science region. The guide regions are at the top and bottom of each CCD and are  $2048 \times 516$  pixels. When the orthogonal transfer shift is not engaged, OPTIC functions as a conventional imager with the guide regions used as science regions. Amplifiers are placed at the end of each chip, therefore the detector conceptually is a square array of four 2K by

2K CCDs. At WIYN, the pixel scale is  $0.14''$ , thus covering an area of  $9.6' \times 9.6'$ . It has a read noise of 4 electrons, a nominal gain of  $1.4 \text{ e/ADU}$ , and a readout time of 25 sec.

The OPTIC frames were designed to have a center-to-corner overlap, centered on the cluster, and covering as much of the P03 data set as possible. For each frame we have typically taken a 600-sec exposure in Harris  $V$  and a 300-sec exposure in Harris  $I$ . One frame at the center of our area had three repeated exposures in each filter, each of the same nominal duration as for the typical observations. Hereafter we will call this frame, the “central-deep field”. The seeing varied between 0.8 to 2 arcsec (in the  $I$  band) during the entire run, therefore our data varies in quality and depth. The central-deep field was observed in  $1.0''$  seeing. Since the purpose of this study was to cover as large an area as possible to match the P03 set, and given that the seeing was rather poor for most of the data, we have used OPTIC without the OT engaged for the entire run.

Each OPTIC frame was divided into its four amplifier subunits, and each subunit was reduced individually. The reduction included standard bias and flat-field corrections. The detection and object classification was performed using the software package SExtractor (Bertin & Arnouts 1996). Instrumental magnitudes were determined with IRAF, using a single aperture, where the radius of the aperture is  $1.5 \times FWHM$ . For the deep field, we have stacked the three exposure after shifting them by  $\sim 1 - 2$  pixels to align them. Saturation sets in between  $V \sim 17$  and 18, depending upon the seeing conditions.

To calibrate our dataset, we chose to use an already standardized dataset of adequate depth and area coverage. The best match was the data from von Hippel & Sarajedini (1998, hereafter vHS98), who have used practically the same  $VI$  filters as we have. The  $I$  filter used by vHS98 is slightly different than the one we have used, since the filter was replaced in 2001. We start the calibration process by using only a constant term in both  $V$  and  $I$  bands, and applying it individually, for each CCD subunit. We begin with the central-deep field calibrated directly on the vHS98 data. Between 14 and 79 stars are used in each CCD subunit to determine the magnitude offsets, using a  $2.5 - \sigma$  clipping of residuals. We obtain a typical scatter of  $\sim 0.04$  in the  $V$  band and  $\sim 0.07$  mags in the  $I$  band. The larger scatter in the  $I$  band than in the  $V$  band is due to a small color term present in the residuals caused by the slight difference in the  $I$  filter used by the vHS98 observations and ours. We therefore redetermine the calibration including a linear color term for the  $I$  band. This is applied for the entire 4 subunit frame using 170 standards. The newly obtained colors are checked with the standard values from vHS98 and no further trends are detected. The linear color term is  $0.055 \pm 0.005$ ; uncertainties in the constant term are of the order of 0.01 mags in both  $V$  and  $I$  bands. Once the central-deep field is calibrated, we use it as a standard field for frames that overlap with it. This calibration process is propagated outward to cover the entire area



shown in Fig.1. Therefore, our data is on the vHS98 photometric system. Final magnitudes per object are determined by averaging multiple measurements when available. The errors are then determined from the scatter of repeated measurements (with  $2.5 - \sigma$  rejection). For single measurements, the errors are those calculated by the IRAF routines. Objects with formal IRAF errors larger than 0.4 magnitudes are not included in the final dataset. The positions are determined separately for each CCD subunit by tying it into the positions from the P03 catalog. The objects are considered matched if they are within  $0.5''$  of each other.

SExtractor’s neural network classifier provides a stellarity index value which can be interpreted as the probability of an object being a point source. Clearly the classification is signal-to-noise dependent, and therefore non-uniform across our area. We chose to use the stellarity index as given by the  $V$  frames, which have twice the exposure time of the  $I$  frames. For multiple measurements, we have also averaged the indices. In what follows, we will proceed carefully with the interpretation of this index and eventually use a statistical approach to remove the contribution of galaxies to the CMD. In Figure 2 we show the magnitude errors in each passband as a function of magnitude for the entire sample (in black), and for the central-deep field (in red). The gray line represents a moving median for the entire sample. The bottom plot shows the stellarity index as a function of magnitude. For the central-deep field, a reliable classification is obtained down to  $V = 22$ , where the distribution is bimodal with peaks near 1 for stars, and near 0 for galaxies. For the entire set, this limit is more difficult to pinpoint due to the inhomogeneous data; however at magnitudes fainter than  $V = 21.5$  the distribution is single peaked.

### 3. Color-Magnitude Diagrams: The Overdensity’s Distance, Metallicity and Age

We show in Figure 3 the  $BV$  CMD from P03 (which covers 0.75 square degrees) and the  $VI$  CMD from our data (which covers 0.37 square degrees). We also present the CMDs generated by the Besancon galactic starcount and kinematic model (Robin et al. 2003), for an area equal to ours, and centered at the location of NGC 188. The top three panels show the  $BV$  CMDs, while the rest show the  $VI$  CMDs for various samples. The top left panel shows the entire P03 stellar sample as classified in that work. The top middle panel shows the P03 sample matched with our data set, i.e. restricted to an area equal to that in our study, and a bright magnitude cut from the OPTIC sample. In this panel we show stars as classified in the current work that achieved a better classification at deeper magnitudes than P03. The top right panel shows the Besancon data. A continuous line is drawn to represent the limiting magnitude of the P03 data. The plots of observed data clearly show an excess

of blue stars between  $V = 19$  and the plate limit, that is not seen in the simulated data. Likewise, NGC 188 is not seen in the simulations and it provides an excellent benchmark to study the newly found overdensity. In the middle row, we show the  $VI$  data for objects with stellar index larger than 0.2 (left), larger than 0.5 (middle) and for the Besancon data (right). An overdensity is apparent roughly between  $V \sim 20$  and 22, and  $(V - I) = 0.5$  to 1.1 when compared to the simulated data. If we apply a more restrictive criterion, i.e., a stellar index larger than 0.8, we practically eliminate the faint part of the data: essentially NGC 188’s main sequence ends at  $V \sim 21.2$ , which is unrealistic. That such a cut causes severe incompleteness of the data, can also be seen from Fig. 2, bottom panel.

The bottom row of the panels shows our data for the central-deep field for the two samples of stellar objects as defined above. This field covers an area of only 0.025 square degrees; however a stellar overdensity appears between  $V = 21$  and 22 at  $(V - I) \sim 1.0$ . The scatter in color at these magnitudes due to measurement errors can be estimated from the scatter in NGC 188’s main sequence for single stars at the same magnitude. It can be seen that the overdensity’s scatter is comparable to that of NGC 188, indicating that we see a main-sequence like feature in this central-deep field. The accuracy of proper motions from P03 for the few objects in this supposed main sequence feature for the central-deep field, is unfortunately inadequate for assigning individual membership probabilities at such faint magnitudes.

In Figure 4 we show the objects counts as a function of  $V$  magnitude for a sample restricted in color to represent the region of the overdensity:  $0.5 \leq (V - I) \leq 1.1$ . We show the counts in our  $VI$  data for the entire sample (gray), for objects with stellar index larger than 0.2 (black), and larger than 0.5 (red). The Besancon star counts are shown with a dotted line, and galaxy counts from the Chandra Deep Field South (Gawiser et al. (2006), and see description below) are shown with a green line. Our data become incomplete at  $V \sim 21.2$ . However, a clear stellar excess is apparent between  $V = 19$  and 21.6 when compared to the Besancon star counts, assuming the conservative stellar index of 0.5. Our newly obtained  $VI$  data thus confirm the existence of a stellar overdensity in the background of NGC 188 that was first seen in the P03 data. While the central-deep field hints to a main-sequence like shape of the overdensity, we further explore this issue with the entire data by doing a statistical subtraction of the galaxies and of the Besancon model starcounts from our  $VI$  CMD.

Before this however, we estimate the overdensity’s distance, metallicity and age. To do so, we use the Dartmouth Stellar Evolution Database (Dotter et al. 2008). First, we fit isochrones by eye in both  $BV$  and  $VI$  CMDs for NGC 188, as a check and reference. From our preliminary trials we found that the Dartmouth models that used the semi empirical

color transformations of Vandenberg & Clem (2003) were a better fit than those that used synthetic color transformations. We have adopted the following well-estimated reddening-related quantities:  $E_{B-V} = 0.09$ ,  $A_V = 0.29$ ,  $E_{V-I} = 0.12$  (vHS98, Sarajedini et al. 1999). For NGC 188, Meibom et al. (2009) have determined a true distance modulus of  $11.24 \pm 0.09$  from an eclipsing binary star. We adopt this distance modulus and a solar metallicity. The best-fit isochrone is a 6.5 Gyr model. We note that we obtained poorer fits in the  $VI$  CMD when we used a distance modulus of 11.4 as derived by vHS98, and Sarajedini et al. (1999).

For the overdensity, we fit isochrones only in the  $BV$  data. We adopt the reddening determined for NGC 188 (see above), thus assuming that there is no reddening between NGC 188 and the overdensity. Since NGC 188 is located 700 pc above the Galactic plane, this is a realistic assumption. We explore four metallicity values:  $[Fe/H] = 0.0, -0.5, -1.0$  and  $-1.5$ . For  $[Fe/H] = -1.0$  and  $-1.5$ , the isochrones are moderately  $\alpha$ -enhanced ( $[\alpha/Fe] = 0.2$ ), to represent a typical halo population. We chose the overdensity’s supposed main sequence turnoff area at  $V \sim 19$  and  $(B - V) \sim 0.5$  as a reference point through which the theoretical isochrones should pass. In Figure 5, we show the isochrones overlaid on the  $BV$  data, with each panel corresponding to one metallicity value. The corresponding age and distance modulus range from 2.5 to 12 Gyr, and from 16.0 to 14.8 mag, and these numbers are specified in each panel. From the four cases, the ones that appear to best fit the data are the two intermediate metallicity ones. We therefore characterize the overdensity to be an intermediate to old population (6 to 10 Gyr) with a metallicity between  $-0.5$  and  $-1.0$ . The estimated distance is thus between 10.0 and 12.6 kpc. We note that this estimation assumes that the overdensity has no depth along the line of sight, which is likely unrealistic. At a fixed metallicity and age, a given depth of the overdensity will produce a composite main sequence with a poorly defined turnoff and insufficient curvature to match the main sequence of a single isochrone. While this may be the case for the  $BV$  data, we can not quantify it properly with the data available so far. On the other hand, we can safely place a lower limit on the distance ( $\sim 10$  kpc) which is most important in the discussion of the plausible orbit of this structure (see Section 5).

In Figure 6 we show the two selected isochrones (in red for  $[Fe/H] = -0.5$ , and blue for  $-1.0$ ) overlaid on the  $BV$  data (top), and on the  $VI$  data with stellar index  $> 0.5$ : all area (middle), and the central-deep field (bottom). NGC 188’s isochrone is also shown (green). We can see that the isochrones determined from the  $BV$  data fit well the  $VI$  data.

Given the inability to properly separate stars from galaxies at magnitudes fainter than  $V \sim 21$  we aim to apply a statistical correction to our  $VI$  CMD. For this purpose, we require a very deep dataset with well-calibrated photometry and good star/galaxy separation down to  $V \sim 23$ . We can then use the CMD of the galaxies in such a dataset to statistically

subtract them from our CMD, assuming galaxies occupy the same region in the CMD. There are numerous multi-band, deep field surveys aimed to study field galaxy population and evolution. One such survey is the Multiwavelength Survey by Yale-Chile (MUSYC)<sup>2</sup> that is focused on four fields. Of these four, we select two well-known fields: the Chandra deep field south (CDFS) at (RA, Dec) = (53.121°, -27.813°) and (l, b) = (224°, -54°), and the Hubble deep field south (HDFS) at (RA, Dec) = (338.148°, -60.787°) and (l, b) = (328°, -49°). The construction of the various catalogs are described in Gawiser et al. (2006) and Taylor et al. (2009). We work with the catalogs based on the *BVR*-detection image that lists fluxes in various passbands including the *VI* bands which are of interest here, and a stellarity index determined with the same software package as in our work. We use the fluxes determined from fixed aperture photometry (with an aperture correction, see Gawiser et al. 2006) rather than other flux estimates more appropriate for galaxies, as we wish to have an observing set resembling ours as much as possible. Fluxes are transformed onto the Vega magnitude system according to the transformations provided in the catalog documentation. These catalogs are complete to  $R \sim 25$ , and cover an area of  $0.5^\circ \times 0.5^\circ$ , or 0.3 square degrees. The star/galaxy separation appears robust to  $V \sim 23$ , where the stellarity index has a well-defined bimodal distribution (Gawiser et al. 2006). We have plotted *VI* CMDs for stars in both fields and compared them with Besancon Galactic field simulations. The range in color and the color location of the blue edge and of the red peak representing disk dwarf stars compare well between the observed and simulated data, assuring us that the photometric calibration is reliable. We then select galaxies (stellarity index  $\leq 0.2$ ) within  $V \leq 23.0$ . We adjust the  $V$  and  $(V - I)$  such that both fields have the reddening of the field of NGC 188. Next, we construct Hess diagrams for the galaxy samples in CDFS and HDFS, and for our entire sample. The galaxy Hess diagrams are scaled *only* by a constant value to adjust for the different spatial area between our data (0.37 sq. deg.) and the CDFS/HDFS area (0.3 sq. deg.). Then we subtract each galaxy Hess diagram from our data. Here we show only the results from the CDFS, as the other field gives similar results.

The results are shown in Figure 7 for the CDFS. Besides the galaxy-subtracted diagram, we also show the subtraction of the Besancon model starcounts from the galaxy-subtracted observed Hess diagram to highlight the stellar overdensities in this field. Thus, the top right panel of Figure 7 shows the Hess diagram of our field with all detected objects included. The top right panel shows the galaxy-subtracted diagram. The bottom left panel shows the Hess diagram of the galaxy-subtracted and Besancon-model subtracted data. NGC 188’s sequence as well as that of the newly found overdensity are clearly visible. The bottom right panel shows the galaxy-subtracted Hess diagram with with the isochrones from Fig. 6

---

<sup>2</sup>[www.astro.yale.edu/MUSYC/](http://www.astro.yale.edu/MUSYC/)

overlaid. The faint part of the overdensity’s main sequence ( $V \sim 21.0$  to  $22.3$ ) is now better defined. Similarly, NGC 188’s faint part of the main sequence is more apparent after the galaxy subtraction. We note that the subtraction over corrects toward the faint end since our data become incomplete at  $V \sim 21.2$ , thus reinforcing the reality of the overdensity. The two isochrones that best characterize this overdensity according to the  $BV$  data are in reasonable agreement with the lower part of the main sequence as seen in the  $VI$  data. While the region of the turnoff is not very well defined in the  $VI$  data, the blue edge of the  $VI$  data is bluer by  $\sim 0.15$  mags in the magnitude range  $V \sim 19.0$  to  $20.0$ , than at brighter magnitudes, hinting to the presence of a turnoff.

The metallicity and age of the stellar population of the overdensity determined here agree reasonably well with other determinations for the stellar populations in the Monoceros stream such as those of Newberg et al. (2002), or more recently by Ivezić et al. (2008). For example, Ivezić et al. (2008) estimate a metallicity of  $-0.95$  with a scatter of  $0.15$  dex from DR6 of the Sloan Digital Sky Survey.

## 4. Proper-Motions: Kinematics of the Overdensity

### 4.1. Identifying the Overdensity in Proper-motion Space

We search the P03 proper-motion data for a kinematically cold, cluster-like structure, other than NGC 188 to confirm that the main-sequence feature in the CMD is indeed a stellar stream. Assuming a velocity dispersion of  $\sim 10$  km s $^{-1}$  for stars in a stellar stream generated from a massive satellite such as Sagittarius dwarf galaxy (Sgr) for instance (Majewski et al. 2004), at a distance of 10 kpc, the expected proper-motion dispersion is  $0.2$  mas yr $^{-1}$ . The proper-motion errors in P03 data do not reach these values at the faint end of the survey where the overdensity is present. Therefore the proper-motion measuring uncertainty will dominate the overall proper-motion dispersion. For the color range of the overdensity, the proper-motion errors in P03 are:  $0.7$  mas yr $^{-1}$  at  $V = 19$ ,  $1.2$  mas yr $^{-1}$  at  $V = 20$ ,  $1.7$  mas yr $^{-1}$  at  $V = 21$ , and  $2.4$  mas yr $^{-1}$  at  $V = 21.4$ . These are mean values of the formal proper-motion errors from P03. We thus search for a kinematically cold structure with a dispersion comparable to the size of the proper-motion errors, which vary substantially at the faint end of the survey.

In Figure 8 we show the relative proper motions from P03. The top left panel shows the proper-motion distribution of the entire P03 stellar sample. The cluster NGC 188 is clearly visible at  $\mu_{\alpha} \cos \delta = -5.3$  and  $\mu_{\delta} = -0.4$  mas yr $^{-1}$  as determined by P03, with a proper-motion scatter  $\sim 0.5$  mas yr $^{-1}$  in agreement with formal proper-motion errors.

Two proper-motion samples are selected within the circles drawn. One is located at the approximate center of the overdensity ( $(\mu_\alpha \cos \delta, \mu_\delta) = (-3.9, 2.9)$  mas yr<sup>-1</sup>, on the relative proper-motion system of P03) with a radius of 1 mas yr<sup>-1</sup>. The second is placed at some arbitrary location to represent a control Galactic field, and its radius is chosen such that both samples have the same number of objects. The middle and bottom left panels show the CMD of these two proper-motion selected samples. The one containing the overdensity shows a well defined main sequence and possibly a subgiant branch, while the control field does not. In the top right panel we show our CMD-selection of stars in the overdensity, and another control sample away from the overdensity, but in the same magnitude range:  $V \geq 19$ . These two samples have similar numbers of objects. The middle and bottom right panels show the proper-motion distributions of the two CMD-selected samples: that including the overdensity, and that excluding it respectively. The middle panel clearly shows a proper-motion clump, while the bottom panel does not. Therefore, we conclude that the stellar overdensity, not only follows a main-sequence like feature in both  $BV$  and  $VI$  CMDs, but also features a kinematically cold population characteristic of tidal stellar streams.

#### 4.2. Absolute Proper Motion of the Overdensity

Next, we want to determine the mean absolute proper motion of the overdensity. To do so, we work with the  $BV$  CMD-selected sample from Fig. 8. First, we re-determine the correction to absolute proper motion in this field using in addition to the 100 galaxies listed by P03, the newly identified ones from our study with stellarity index  $\leq 0.2$ . We limit the galaxy sample to objects brighter than  $V = 21.0$  and with proper-motion errors in both coordinates less than 2 mas yr<sup>-1</sup>. We also eliminate proper-motion outliers, and finally obtain a sample of 143 galaxies. These galaxies average relative proper motion, also known as the zero-point correction is  $\mu_\alpha \cos \delta = -2.83 \pm 0.18$  mas yr<sup>-1</sup> and  $\mu_\delta = -1.05 \pm 0.17$  mas yr<sup>-1</sup>. In the P03 study, the stellar proper motions were corrected for magnitude equation relative to cluster members with  $V = 16.0$  (their Fig. 2). However P03 chose not to apply this rather strong magnitude equation to the galaxies, as they showed no detectable trend in their proper motions with magnitude. For the purpose of determining the absolute proper motion of the overdensity, we have chosen to work with the data from P03 but *uncorrected* for magnitude equation. Our choice is justified by the fact that in P03 the magnitude equation in proper motions is poorly constrained at  $V > 19$ . At these magnitudes it was difficult to select reliable cluster members from the  $BV$  CMD which were used to derive the magnitude equation. We inspect the proper motions of galaxies (including the fainter ones identified in this work) as a function of magnitude, as well as the proper motions of the CMD-selected overdensity stars as a function of magnitude. We detect a very small trend

with magnitude in  $\mu_\delta$ . This trend is about  $0.2 \text{ mas yr}^{-1}\text{mag}^{-1}$  and is similar for galaxies and for stars in the overdensity. The average magnitude for galaxies is  $V = 19.9$  and that of stars in the overdensity is  $V = 20.4$ . The combination of the small difference between the mean magnitude of the two samples and their similar magnitude trend allows us to safely proceed with no magnitude equation correction to either galaxies or overdensity stars.

To determine the mean absolute proper motion of the overdensity, we apply the well-known techniques developed for open-cluster studies that separate the cluster population from the Galactic field population. Here we follow the procedure described in Girard et al. (1989) where both the cluster and the field have their intrinsic proper-motion distributions described by Gaussians. Typically, observed proper-motion distributions are built in each coordinate and fitted with a sum of two Gaussians representing the field and the cluster. The width of the Gaussian distribution for the cluster reflects the intrinsic dispersion of the cluster, the measuring uncertainty of the proper motions and a contribution due to the smoothing process done when constructing the observed distributions (for details see Girard et al. 1989, Dinescu et al. 1996). The analysis is simple when the proper-motion errors have approximately the same value. However, in our case the proper-motion errors vary significantly with magnitude. For such cases, as shown by Girard et al. (1989) it is better to construct an error function from the formal proper-motion errors. This error function is convolved with the function describing the intrinsic proper-motion distribution of the cluster (and field), which in this case is taken to be a Gaussian, and then fitted to the observed proper-motion distribution. The parameters from the fit are the number of cluster stars, the mean proper motion of the cluster and of the field and the intrinsic dispersion of the cluster and of the field. We have tried various fits for our sample by experimenting with the size of the formal proper-motion errors (i.e., increasing them by 25%) and with the number of stars in the overdensity. In all these fits, the mean motion of the overdensity appears with a robust determination and a variation of  $\sim 0.2 \text{ mas yr}^{-1}$ . The mean absolute proper motion of the overdensity is  $\mu_\alpha \cos \delta = -1.48 \pm 0.27$  and  $\mu_\delta = 1.98 \pm 0.26 \text{ mas yr}^{-1}$ , where the final error includes the contribution from the variation in the fit and that from the absolute proper-motion zero point. From the fits, we also obtain approximately 200 stars as members of the overdensity from a total of 482 stars in the CMD-selected sample. In Galactic coordinates, the proper motion is  $\mu_l \cos b = -1.40 \pm 0.27$  and  $\mu_b = 2.04 \pm 0.26 \text{ mas yr}^{-1}$ .

## 5. Discussion

### 5.1. The Overdensity as Part of the Monoceros Stream

The overdensity is located at  $(l, b) = (122.8^\circ, 22.5^\circ)$ . In what follows, we will work with two values for the distance to the overdensity determined in Section 3: 10.0 and 12.6 kpc. For 10 kpc, the overdensity is at  $(X, Y, Z) = (13.0, 7.8, 3.8)$  kpc, while for 12.6 kpc it is at  $(X, Y, Z) = (14.3, 9.8, 4.8)$  kpc, where the Sun is at  $(X, Y, Z) = (8, 0, 0)$  kpc. Besides the properties of the stellar population, another hint that this overdensity may belong to the Monoceros stream is its Galactic location. Of the numerous studies that have sampled this structure, here we mention those that have found positive detections near our region: Rocha-Pinto et al. (2003) analyze M giants from 2MASS to map out this structure; indeed they find positive detections at  $(l, b) \sim (130^\circ, 26^\circ)$  with an inferred heliocentric distance between 9 and 13 kpc. Conn et al. (2005) trace the main sequence of Mon using the Wide Field Camera on the Isaac Newton Telescope. They find a positive detection at  $(l, b) = (118^\circ, 16^\circ)$  and at a heliocentric distance of  $\sim 12$  kpc. Momany et al. (2006) investigate an alternative explanation of the overdensity at the Galactic location of the Conn et al. detection, namely the flared disk. Their model of the warped and flared disk is based on 2MASS red clump and red giant stars. For this Galactic location, Momany et al. provide a map of the scale height of the flared disk as a function of distance from the Galactic plane and from the Galactic center. This map is the closest in direction, of those presented, to our NGC 188 field. In this map our overdensity, for both distance determinations, is located beyond the contour corresponding to  $3\times$  the scale height of the flared disk. Therefore, its position alone makes the overdensity unlikely to belong to the flared disk as recently modeled by Momany et al. (2006).

In order to provide further evidence for this tentative identification, we compare our distance estimation and proper motion to the predictions of the Peñarrubia et al. (2005, hereafter P05) model for the Monoceros stream. This model describes the disruption of a satellite on a prograde, low inclination, low eccentricity orbit and is constrained by spatial distribution, distance estimates and radial velocities in overdensities mapped above and below the Galactic plane and between  $l = 110^\circ - 240^\circ$ . In Figure 9, we show the spatial distribution of the debris from the P05 model (top panel). The location of our field is marked (red symbol), and a sample of model particles selected within  $4^\circ \times 4^\circ$  centered around our field are also shown (black squares). The middle and bottom panels show the proper motions in Galactic longitude and latitude as a function of distance for the entire model (grey), for the particle sample coincident with our field (squares) and for our field (red). The model indicates that there are two distance groups, one at  $\sim 9 - 12$  kpc, and the other at  $17 - 23$  kpc. The near group, which corresponds well with our data divides into two groups according



to the proper motion in latitude: one group moves downward, toward the Galactic plane, the other, away from the plane. Our data fits very well with the group moving away from the plane. Located at a distance of 3.8/4.8 kpc from the plane, stars in this overdensity will continue to get further away from the plane as they proceed in a prograde sense. We have found no evidence in the proper-motion data of the other group postulated by the model, i.e. the one moving toward the plane. Likewise, we find no evidence in our data of the more distant group at 20 kpc, which may be due to the magnitude limit of our observations.

## 5.2. Plausible Orbits

As we do not have a measurement of the radial velocity (RV) for stars in the overdensity, we explore a range of plausible values in order to have a better understanding of the likely orbits constrained by the absolute proper motion and by the distance estimate. From the Besancon model, stars in the color ( $B - V < 1.0$ ) and magnitude ( $17 < V < 22$ ) ranges occupied by the overdensity have a heliocentric RV distribution centered at  $\sim -70 \text{ km s}^{-1}$ , with a FWHM of  $140 \text{ km s}^{-1}$ , and a tail toward negative values of  $\sim -300 \text{ km s}^{-1}$ . We therefore choose the following RV values to be explored: 0, -70, -140 and -300  $\text{km s}^{-1}$  and two extreme values of 100 and -400  $\text{km s}^{-1}$ . In Table 1 we list the adopted heliocentric RV, and the resulting velocity components in cylindrical coordinates ( $\Pi, \Theta, W$ ). We also list the maximum distance from the plane and the eccentricity of the respective orbits. The adopted peculiar velocity of the Sun is from Dehnen & Binney (1998). The velocity of the local standard of rest is  $(\Pi, \Theta, W) = (0, 220, 0) \text{ km s}^{-1}$ . We have integrated the orbit in the Johnston et al. (1995) Galactic potential.

In all cases explored here that cover the entire plausible RV-range, the orbit is prograde. Also, the maximum distance above the plane is rather high, thus making the orbits unlikely to represent material in the warped or flared disk as described by Momany et al. (2006) for instance. For the 12.6 kpc distance estimate, the orbits are even more inconsistent with a thick-disk origin of this overdensity than for the 10-kpc distance estimate, as the material travels quite far from the Galactic plane.

The orbit with the lowest height above the plane (i.e. 4.2 kpc, for the 10.0 kpc distance estimate) has a highly eccentric orbit, again inconsistent with material belonging to the thick disk. To achieve an orbit more confined to the Galactic plane, for instance within  $\pm 3$  kpc from the Galactic plane we require a distance to the overdensity of 7 kpc for our measured absolute proper motion. This implies a brighter turnoff by  $\sim 0.8$  mag, which the  $BV$  data do not support.

Table 1: Plausible Orbits for the Newly Found Structure

$V_r$ ( $\text{km s}^{-1}$ )	d = 10.0 kpc					d = 12.6 kpc				
	$\Pi$ ( $\text{km s}^{-1}$ )	$\Theta$ ( $\text{km s}^{-1}$ )	W	$z_{max}$ (kpc)	e	$\Pi$ ( $\text{km s}^{-1}$ )	$\Theta$ ( $\text{km s}^{-1}$ )	W	$z_{max}$ (kpc)	e
0	44	241	99	7.3	0.27	43	250	123	11.0	0.34
-70	-14	212	72	5.8	0.03	-17	225	96	9.0	0.13
-140	-72	184	46	5.0	0.23	-77	200	69	8.0	0.19
-300	-205	118	-16	4.2	0.70	-213	142	8	7.6	0.66
100	126	282	137	11.7	0.59	128	286	161	18.2	0.64
-400	-288	77	-54	5.2	0.89	-298	106	-30	9.1	0.86

However, some of the orbits explored here ( $RV = 0$  to  $-140 \text{ km s}^{-1}$ ) are quite compatible with the one proposed by P05 for the model of the Monoceros stream. Therefore, the orbits discussed in combination with the properties of the stellar population of the newly found overdensity argue in favor of its membership to the Monoceros stream.

## 6. Summary

We present evidence for a stellar overdensity in the background of the open cluster NGC 188. By fitting the main-sequence of the overdensity with isochrones in the  $BV$  CMD we constrain its stellar population to be between 6 and 10 Gyr and with a metallicity  $[\text{Fe}/\text{H}] = -0.5$  to  $-1.0$ . The corresponding distance from Sun is between 10 and 12.6 kpc. In proper-motion space, it is shown to be a kinematically cold population. The absolute proper motion, distance and Galactic location of the overdensity agree reasonably well with the predictions of the P05 model for the formation of the Monoceros stream. We also derive plausible orbits by adopting a range of RVs and show that the orbits are incompatible with material belonging to the warp or flare of the disk.

We thank Jorge Peñarrubia for making available to us the simulated data for the Monoceros stream model. Financial support from National Science Foundation through grant AST 04-06884 for this research is acknowledged. I. Platais gratefully acknowledges support from the NSF through grant AST 09-08114 to Johns Hopkins University.

*Facilities:* WIYN 3.5m.

## REFERENCES

- Bertin, E. & Arnouts, S. 1996, *A&AS*, 117, 393
- Casetti-Dinescu, D. I., Majewski, S. R., Girard, T. M., Carlin, J. L., van Altena, W. F., Patterson, R. J., & Law, D. R. 2006, *AJ*, 132, 2082
- Casetti-Dinescu, D. I., Carlin, J. L., Girard, T. M., Majewski, S. R., Peñarrubia, J. & Patterson, R. J. 2008, *AJ*, 135, 2013
- Casetti-Dinescu, D. I., Girard, T. M., Majewski, S. R., Vivas, A. K., Wilhelm, R., Carlin, J. L., Beers, T. C., & van Altena, W. F. 2009, in press
- Conn, B. C, Lewis, G. F., Irwin, M. J., Ibata, R. A., Ferguson, A. M. N., Tanvir, N., & Irwin, J. M. 2005, *MNRAS*, 362, 475
- Conn, B. C., et al. 2007, *MNRAS*, 376, 939
- Conn, B. C., Lane, R. R., Geraint, L. F., Irwin, M. J., Ibata, R. A., Martin, N. F., Bellazzini, M., & Tuntsov, A. V. 2008, *MNRAS*, 390, 1388
- Dehnen, W & Binney, J. 1998, *MNRAS*, 294, 429
- Dinescu, D. I., Girard, T. M., van Altena, W. F., Yang, T-G., Lee, Y-W. 1996, *AJ*, 111, 1205
- Dinescu, D. I., Girard, T. M., & van Altena, W. F. 1999, *AJ*, 117, 1792
- Dinescu, D. I., Majewski, S. R., Girard, T. M., & Cudworth, K. M. 2000, *AJ*, 120, 1892
- Dinescu, D. I., Girard, T. M., van Altena, W. F., & López, C. E. 2005, *ApJ*, 618, L25
- Dotter, A., Chaboyer, B., Jevremović, D., Kostov, V., Baron, E. & Ferguson, J. W. 2008, *ApJS*, 178, 89
- Gawiser, E. et al. 2006, *ApJS*, 162, 1
- Girard, T. M., Grundy, W., López, C. E. & van Altena, W. F. 1989, *AJ*, 98, 227
- Ibata, R., Gilmore, G., Irwin, M. J. 1994, *Nature*, 370, 194
- Ibata, R., Lewis, G. F., Irwin, M. J., Totten, E., Quinn, T. 2001, *ApJ*, 551, 294
- Ivezić Z. et al. 2008, *ApJ*, 684, 287
- Jacoby, G., Tonry, J. L., Burke, B. E., Claver, C. F., Starr, B., Saha, A., Luppino, G. A., & Harmer, C. 2002, *SPIE*, 4836, 217

- Johnston, K. V., Spergel, D. N., & Hernquist, L. 1995, *ApJ*, 451, 598
- Jurić, M. et al. 2008, *ApJ*, 673, 864
- Majewski, S. R., Skrutskie, M. F., Weinberg, M. D., & Ostheimer, J. C., 2003, *ApJ*, 599, 1115
- Majewski, S. R., Kunkel, W. E., Law, D. R., Patterson, R. J., Polak, A., Rocha-Pinto, H. J., Crane, J. D., Frinchaboy, P., Hummels, C. B., Johnston, K. V., Rhee, J., Skrutskie, M. F., & Weinberg, M. 2004, *AJ*, 128, 245
- Meibom, S., Grundhal, F., Clausen, J. V., Mathieu, R. D., Frandsen, S., Pigulski, A., Narwid, A., Steslicki, M., & Lefever, K. 2009, *AJ*, 137, 5086
- Momany, Y., Zaggia, S., Gilmore, G., Piotto, G., Carraro, G., Bedin, L. R., & De Angeli, F. 2006, *A&A*, 451, 515
- Newberg, H. et al. 2002, *ApJ*, 569, 245
- Peñarrubia, J., Martínez-Delgado, D., Rix, H. W., Gómez-Flechoso, M. A. (P05)
- Platais, I., Kozhurina-Platais, V., Mathieu, R. D., Girard, T. M., & van Altena, W. F. 2003, *AJ*, 126, 2922 (P03)
- Robin, A. C., Reylé, C., Derrière, S., & Picaud, S. 2003, *A&A*, 409, 523
- Rocha-Pinto, H. J., Majewski, S. R., Skrutskie, S. R., & Crane, J. D. 2003, *ApJ*, 594, 115
- Taylor, E. N., et al. 2009, *ApJS*, 183, 295
- Tonry, J. L., Burke, B. E., & Schechter, P. L. 1997, *PASP*, 109, 1154
- VandenBerg, D. A., & Clem, J. L. 2003, *AJ*, 126, 778
- Vivas, A. K., & Zinn, R. 2003, *Mem. Soc. Astron. Italiana*, 74, 928
- von Hippel, T. & Sarajedini, A. 1998, *AJ*, 116, 1789
- Yanny, B. et al. 2003, *ApJ*, 588, 824

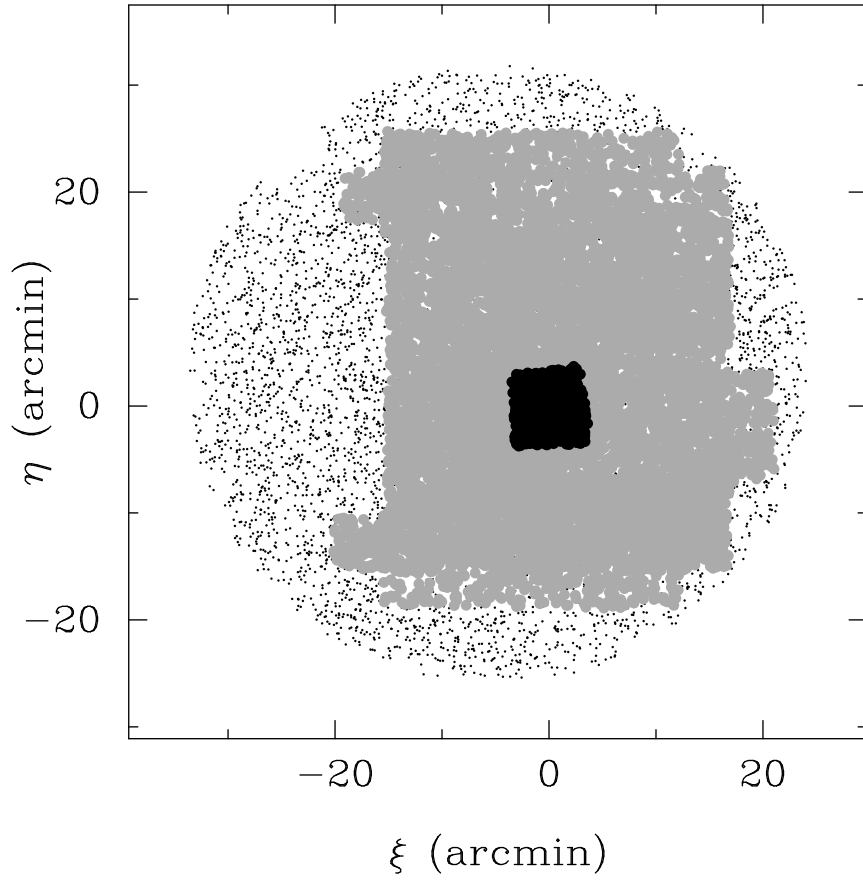


Fig. 1.— Area coverage of various datasets used in this paper: the P03 proper-motion data (black dots), the OPTIC data (grey), and the Von Hippel & Sarajedini (1998) calibrating data set (black filled circles).

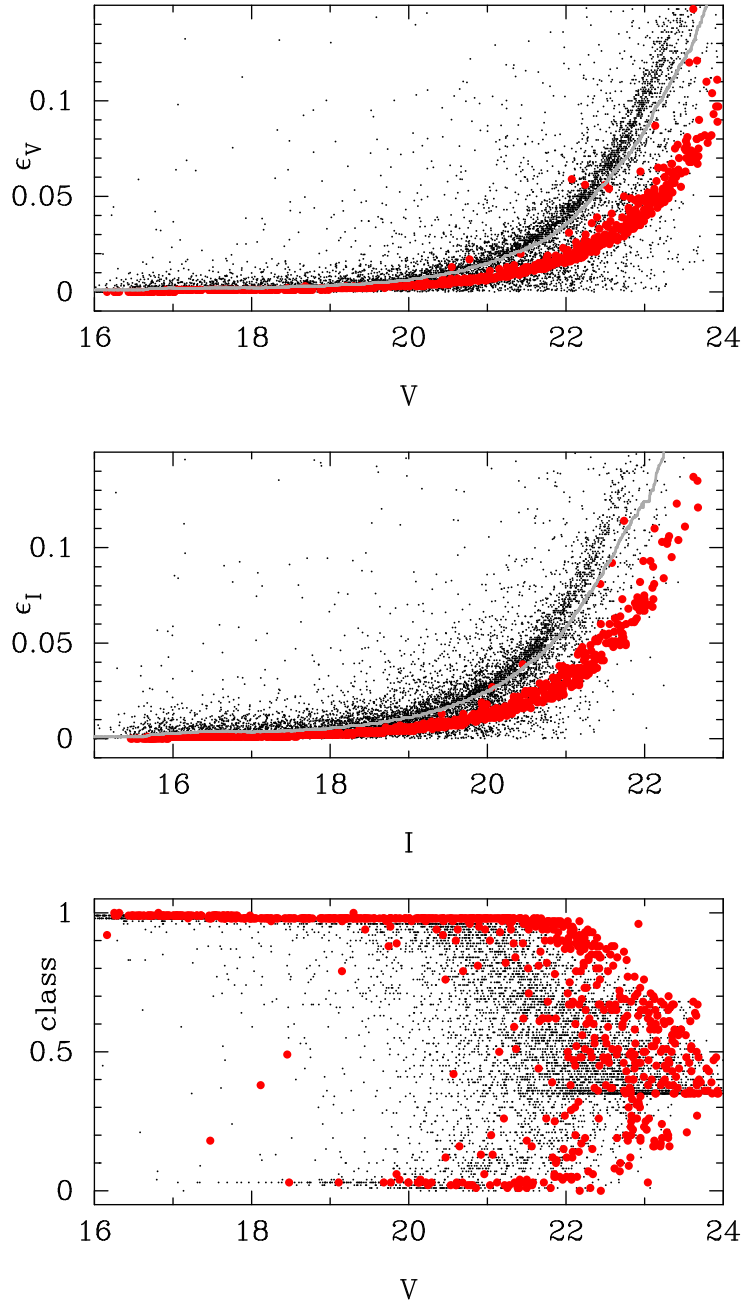


Fig. 2.— Magnitude errors in  $V$  (top) and  $I$  (middle), and stellar index as a function of magnitude (bottom). The gray line shows a moving median for the entire sample. The red symbols show the data for the central-deep field.

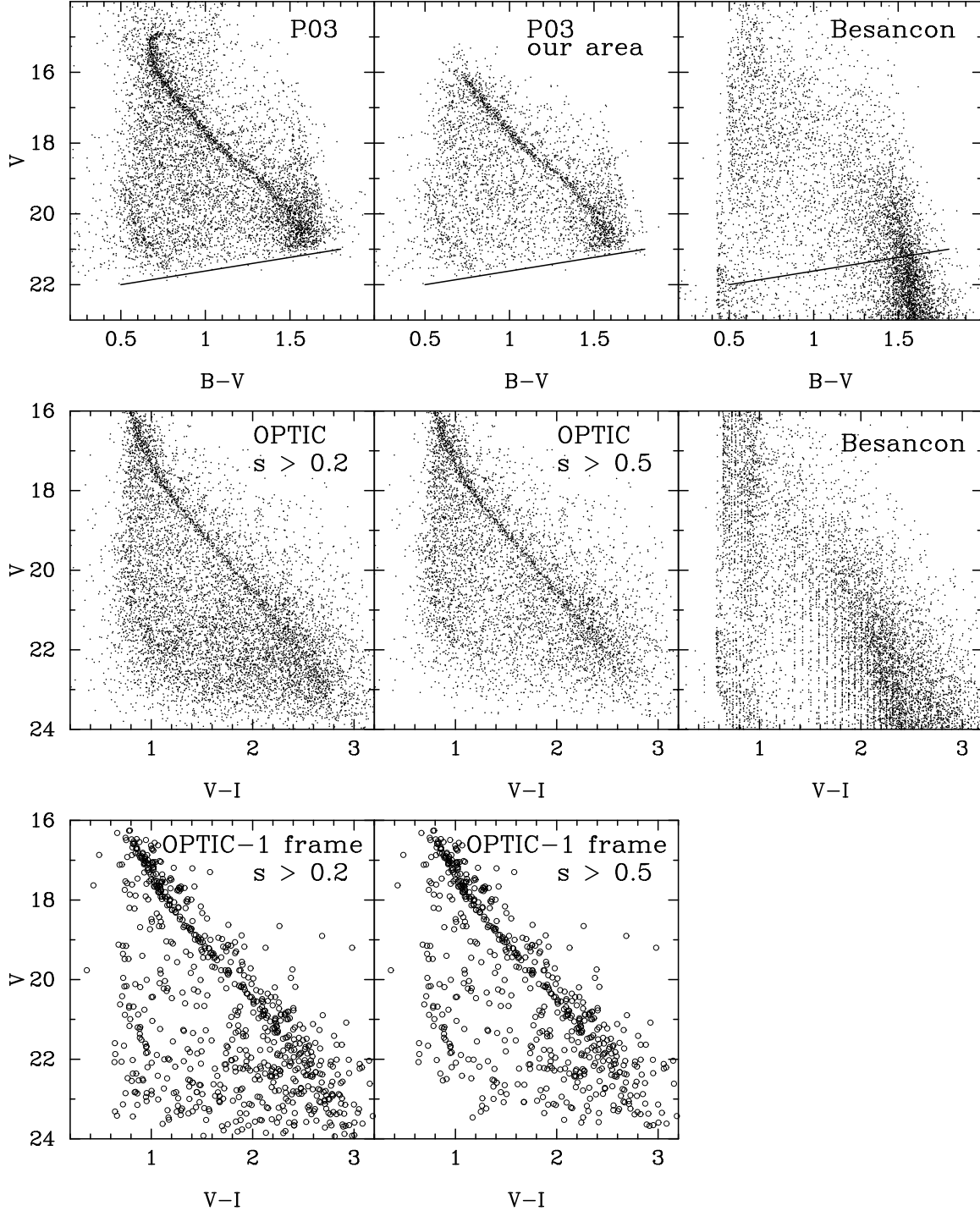


Fig. 3.— Top panels:  $BV$  CMDs of stars in P03 (left), in P03 data restricted to our area (middle), and as predicted by the Besancon model (right) in the same area as that covered by our study. The middle panels show the  $VI$  CMDs of our stellar sample where the stellar index is  $> 0.2$  (left),  $> 0.5$  (middle), and of the Besancon model (right). The bottom panels show the CMDs for stars in the central-deep field, where the stellar index is  $> 0.2$  (left) and  $> 0.5$  (middle).

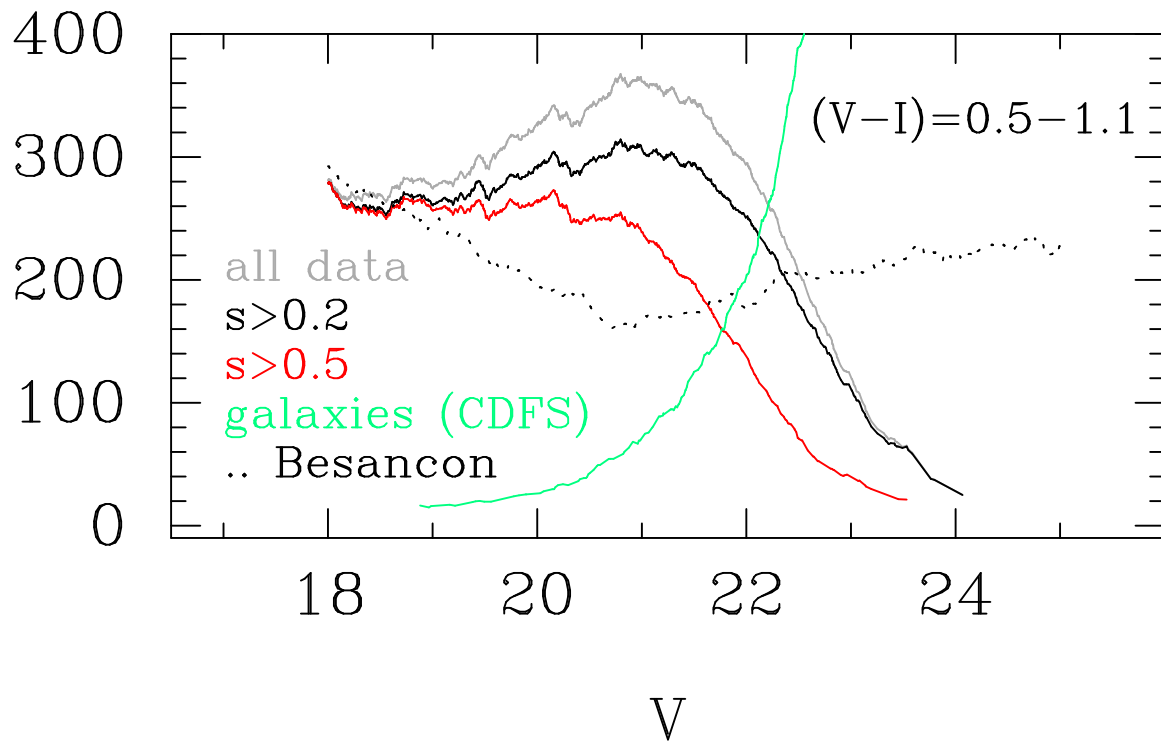


Fig. 4.— Object counts for  $0.5 \leq (V - I) \leq 1.1$  as a function of  $V$  magnitude for our data: all sample - gray, stellar index  $> 0.2$  - black, stellar index  $> 0.5$  - red, for the Besancon model - dotted, and for galaxies(CDFS) - green.



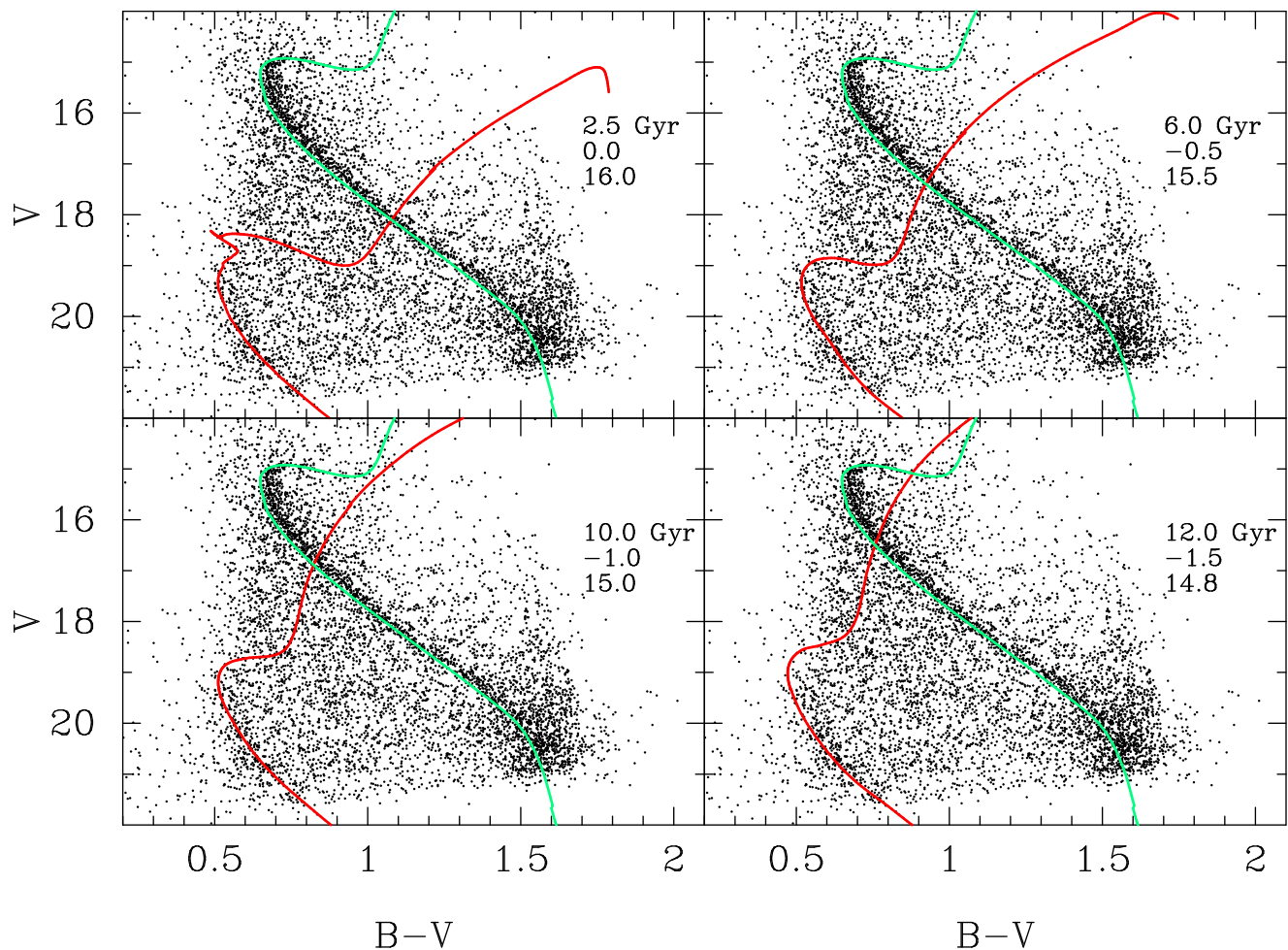


Fig. 5.— Dartmouth isochrones fit to the  $BV$  CMD data. For NGC 188 we used a 6.5 Gyr model of solar metallicity (green). The adopted reddening is  $E_{B-V} = 0.09$ . For the overdensity we show isochrones (red) of four metallicity values. These values together with the age and distance modulus are specified in each panel.

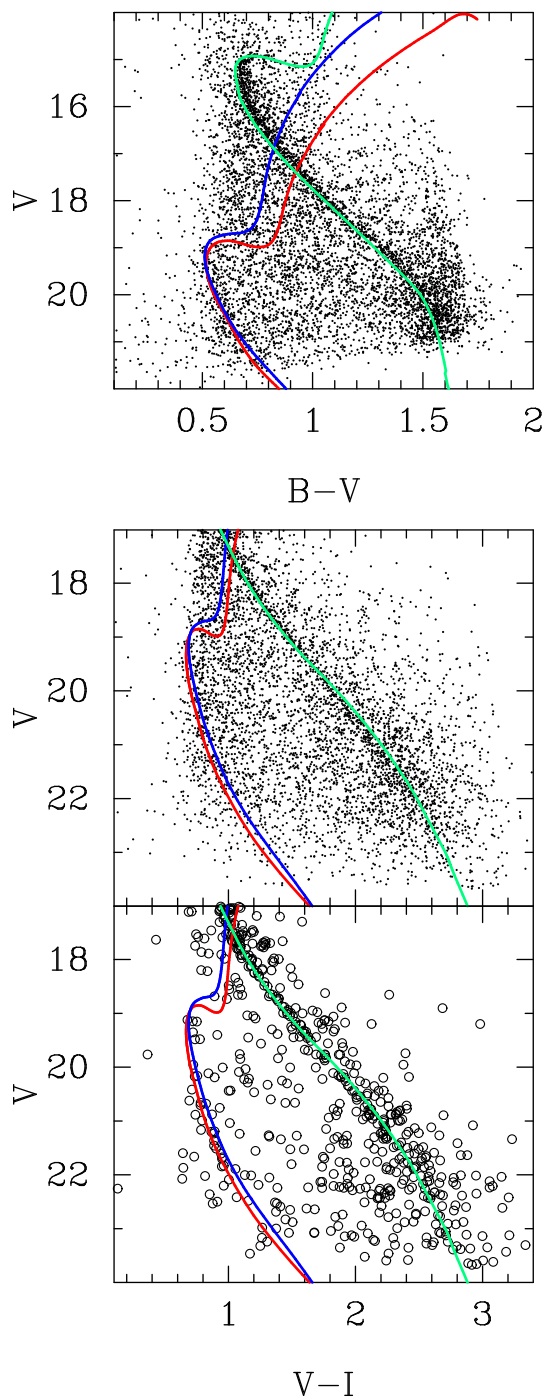


Fig. 6.— Dartmouth isochrones overlaid on the  $BV$  CMD data (top) and on the  $VI$  data (middle) and central-deep field (bottom). In the  $VI$  data objects with stellar index  $> 0.5$  are shown. For the overdensity, we use 6 Gyr models with  $[Fe/H] = -0.5$  (red), and 10 Gyr with  $[Fe/H] = -1.0$  (blue), with distance moduli of 15.5 and 15.0 respectively.

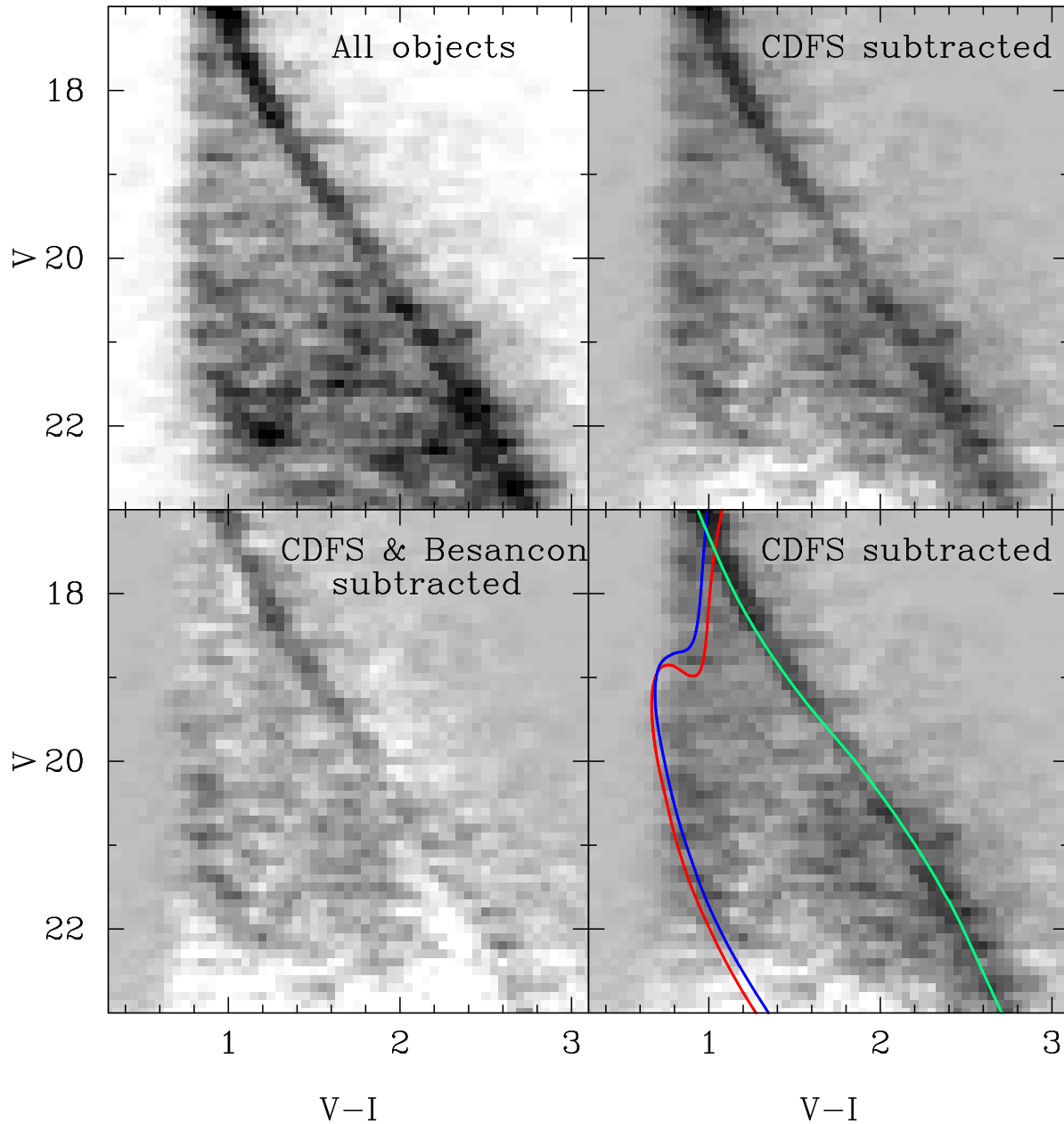


Fig. 7.— Statistical subtraction of galaxies and of the Besancon model from the observed CMD. The galaxies are from the MUSYC survey for the CDFS area. Our entire sample is shown in the top-left panel, the galaxy-subtracted one is in the top-right panel. The bottom-left panel shows the galaxies and Besancon starcount data subtracted from the observed CMD. In the bottom-right panel we show the galaxy-subtracted sample with the isochrones from Fig. 6 overlaid.

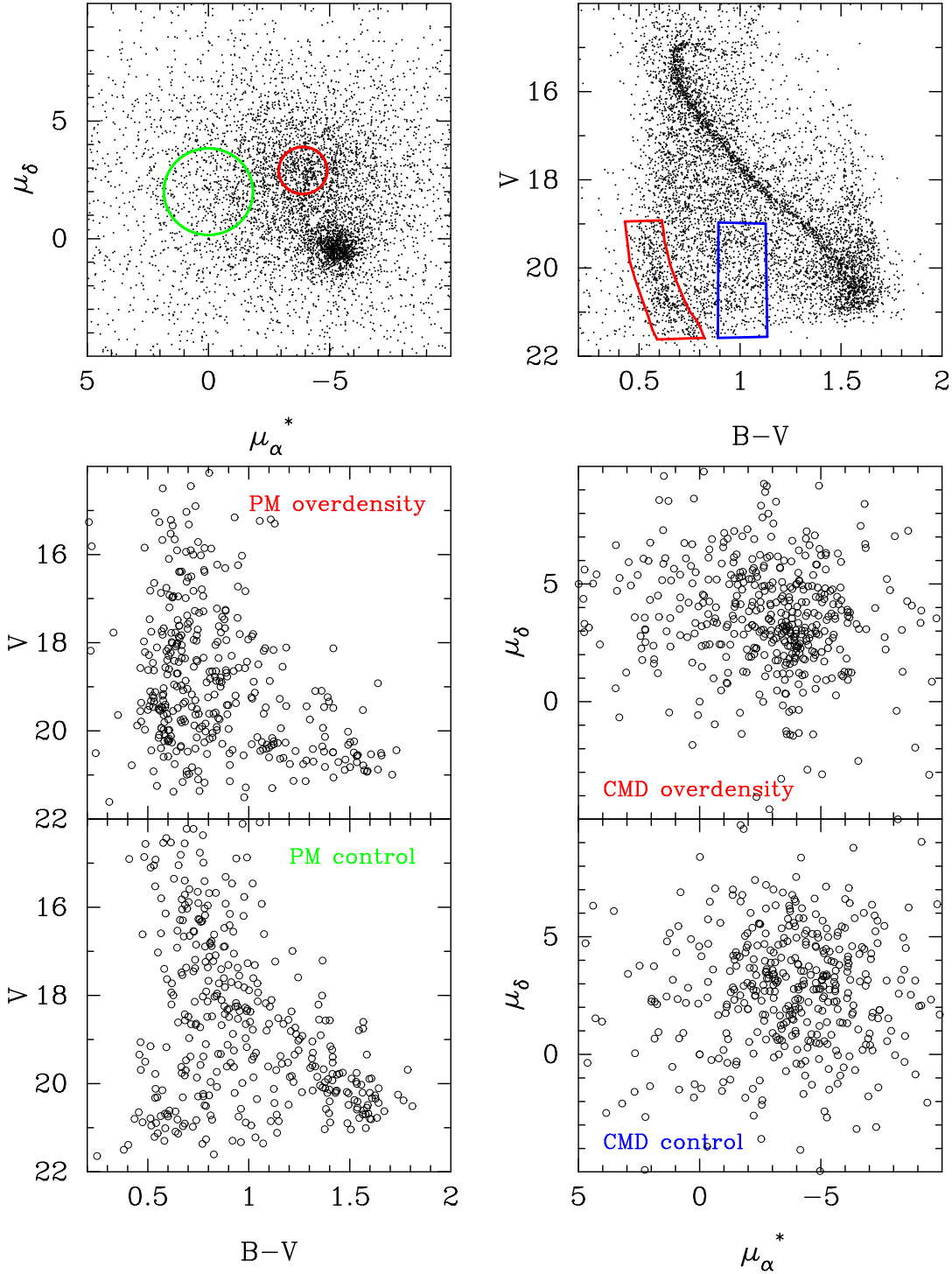


Fig. 8.— Relative proper-motion diagram showing all stars in the P03 data (top-left). The obvious concentration of stars represents NGC 188. Two proper-motion samples are selected from this diagram within the circles shown. The circles include samples of same number of objects. One is centered on the overdensity region, the other on a control region. The middle and bottom left panels show the CMD for the proper-motion selected samples. The top-right panel shows the CMD-selection of two samples: one representing the overdensity, and the other a control Galactic field. The middle and bottom right panels show the proper-motion diagrams of these two samples. The overdensity sample shows a clear proper-motion clump,

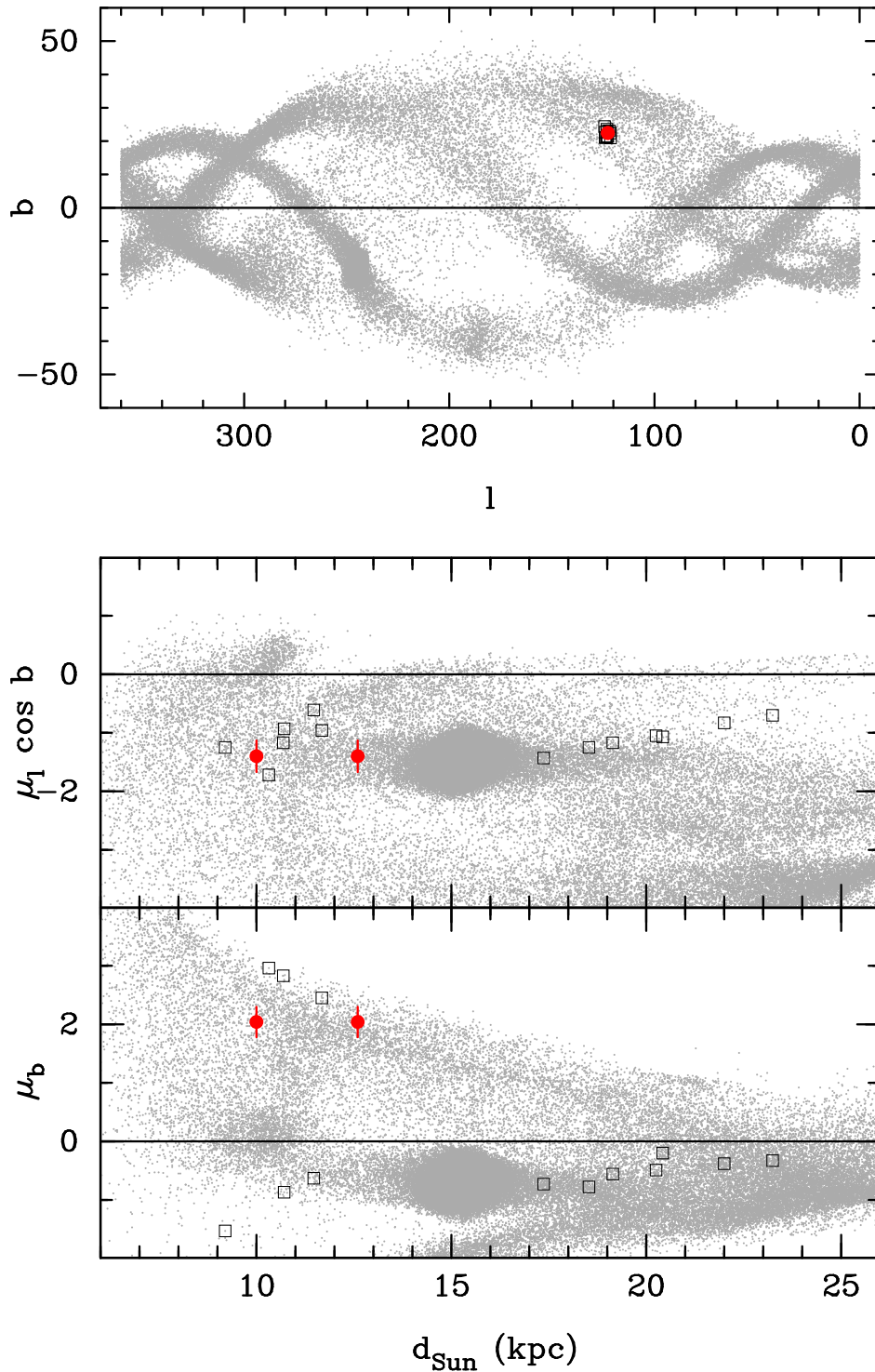


Fig. 9.— Comparison of the Peñarrubia et al. (2005) model for the disruption of the progenitor satellite of the Mon ring with the proper-motion data. The top panel shows the distribution in Galactic coordinates of the model (gray), our field for two distance estimates (red), and a sample from the model representing our field (black open squares). The middle and bottom panels show the proper motions in Galactic coordinates as a function of distance from the Sun. Again, the black open squares show the predicted kinematics at a pointing corresponding to our field. The mean proper motion of the overdensity and its distance agree with predictions from the model for the more nearby part of the stream that merges away